

Journal of Materials Chemistry A

Accepted Manuscript



This is an *Accepted Manuscript*, which has been through the Royal Society of Chemistry peer review process and has been accepted for publication.

Accepted Manuscripts are published online shortly after acceptance, before technical editing, formatting and proof reading. Using this free service, authors can make their results available to the community, in citable form, before we publish the edited article. We will replace this *Accepted Manuscript* with the edited and formatted *Advance Article* as soon as it is available.

You can find more information about *Accepted Manuscripts* in the [Information for Authors](#).

Please note that technical editing may introduce minor changes to the text and/or graphics, which may alter content. The journal's standard [Terms & Conditions](#) and the [Ethical guidelines](#) still apply. In no event shall the Royal Society of Chemistry be held responsible for any errors or omissions in this *Accepted Manuscript* or any consequences arising from the use of any information it contains.

Popcorn-like PtAu nanoparticles supported on reduced graphene oxide: Facile synthesis and catalytic applications

Jie-Ning Zheng,^a Shan-Shan Li,^a Xiaohong Ma,^b Fang-Yi Chen,^a Ai-Jun Wang,^{a*} Jian-Rong Chen,^a Jiu-Ju Feng,^{a*}

^a College of Chemistry and Life Science, College of Geography and Environmental Science, Zhejiang Normal University, Jinhua, 321004, China

^b State Key Laboratory of Multiphase Complex Systems, Institute of Process Engineering, Chinese Academy of Sciences, Beijing 100190, China.

*Corresponding author: jjfeng@zjnu.cn (JJF), ajwang@zjnu.cn (AJW).

Abstract

Popcorn-like PtAu nanoparticles were fabricated by a facile and green one-pot wet-chemical method, where H_2PtCl_4 and HAuCl_4 were simultaneously reduced by glucosamine in alkaline media. The PtAu nanoparticles were further supported on reduced graphene oxide by simple ultrasonication. The nanocomposites showed the enhanced catalytic performances toward oxygen reduction reaction (ORR), dominated by a four-electron pathway, in comparison with the Pt-rGO and commercial 10% Pt/C catalysts. Meanwhile, the nanocomposites displayed the improved electrocatalytic property and better stability for methanol oxidation over Pt-rGO and commercial Pt/C catalysts.

Keywords: Reduced graphene oxide, popcorn-like PtAu nanoparticles, glucosamine, oxygen reduction reaction, methanol

1. Introduction

Bimetallic nanoparticles have attracted significant interest because of their porous and open structures, large surface areas, and abundant active sites exposed on the branched surfaces.¹⁻⁶ Their formation process closely depends on slow nucleation and fast growth, which could be precisely controlled by varying the experimental conditions. Shi et al. fabricated Au-Pd alloy nanodendrites using ascorbic acid as a reducing agent and found that dropwise adding the precursor solution is essential in their work.⁷ John et al. prepared the branched Pd nanostructures in a solution phase reaction at room temperature, and noticed that control over the reaction kinetics was feasible by varying the kinds of surfactants.⁸

Among the bimetallic nanoparticles, PtAu alloy nanostructures have been extensively explored as excellent catalysts for a variety of reactions.⁹⁻¹² Their promising applications prompt their morphology- and size-controlled synthesis. However, only several good examples are found in the literature. For example, Han et al. synthesized Au@Pt heteronanostructures with Pt rough shells as superior catalysts in oxygen reduction reaction (ORR), using Au nanocubes and nanorods as structure-directing seeds.¹³ Guo and coworkers developed a one-step route for construction of Au@Pt core-shell nanodendrites at room temperature.¹¹ Kim's group synthesized PtAu alloy nanotubes with the improved electrocatalytic performance for formic acid oxidation, using Ag nanowires as sacrificial templates.¹²

The PtAu nanocrystals have indeed demonstrated the better activity in the catalytic reaction.¹⁴⁻¹⁶ However, their large-scale commercial applications are severely

impeded by the high cost and easy agglomeration during repeat use.¹⁷ Fortunately, these problems can be easily overcome by the development of graphene science.¹⁸ Specifically, graphene can be used as a suitable carbon support to load metal catalysts including Pt,¹⁹ Pd,²⁰ PdAu,²¹ and PdAg,²² owing to its two dimensional nanostructure, high electrical conductivity, extremely large specific surface area, and superior chemical property.²³

In this work, popcorn-like PtAu nanoparticles were efficiently formed with glucosamine as a reducing agent in alkaline media and further loaded on reduced graphene oxide (rGO) by ultrasonication. The electrocatalytic performance of the as-prepared nanocomposites was examined for ORR and methanol oxidation.

2. Experimental section

2.1 Chemicals

Graphite powders (8000 meshes), chloroplatinic acid (H_2PtCl_6), chlorauric acid (HAuCl_4), glucosamine hydrochloride, polyvinylpyrrolidone (PVP), and commercial 10% Pt/C catalyst were purchased from Aladdin Industrial Corporation (Shanghai, China). Other chemicals were of analytical grade and used without further purification. All the aqueous solutions were prepared with twice-distilled water in the whole experiments.

2.2 Preparation of reduced graphene oxide

In this work, graphene oxide (GO) was prepared from natural graphite powder

via acid-oxidation based on a modified Hummers' method.²⁴ The GO was dispersed in water under ultrasonication, resulting in a yellow-brown aqueous suspension, followed by the addition of freshly prepared NaBH₄ solution (10 mM) to obtain reduced graphene oxide (rGO). After reduction, the color quickly changed to black.

2.3 Synthesis of the PtAu-rGO

For the typical experiment, 100 μL of rGO (1 mg mL⁻¹) and 400 μL PVP (0.25 wt%) were subsequently put into 2 mL water under stirring. Next, 51.8 μL of H₂PtCl₆ (38.62 mM) and 82.4 μL of HAuCl₄ (24.28 mM) were simultaneously added into the mixture under gentle agitation, followed by the ultrasonication for 30 min (the molar ratio of the Pt/Au precursors is 1:1). Afterwards, 2.4 mL of glucosamine was put into the mixed solution. The pH of the system was adjusted to 9 by dropwise addition of the freshly prepared KOH (1.0 M) under vigorous stirring. The color turned black brown within 3 min. The products were collected by centrifugation, and washed thoroughly with ethanol and water, and dried in a vacuum at ambient temperature for the following characterization. To obtain rGO supported PtAu nanocomposites, the PtAu nanoparticles were mixed with 2 mL of the as-prepared rGO solution (1.0 mg mL⁻¹) under ultrasonication. The final products were obtained by drying in a vacuum at ambient temperature.

For comparison, either H₂PtCl₆ or HAuCl₄ was used as a precursor in control experiments, rGO-supported Pt or Au nanoparticles was prepared in a similar way, denoted as Pt-rGO or Au-rGO, while other conditions were kept the same.

2.3 Characterization

The morphology and chemical composition of the samples were determined by JEM-2010 high resolution transmission electron microscopy (HR-TEM) coupled with an energy-dispersive X-ray spectrometer (EDS, Oxford-1NCA) at an acceleration voltage of 200 kV. High angle annular dark-field scanning TEM (HAADF-STEM) imaging and elemental mappings were recorded on a scanning transmission electron microscope (STEM). The oxidation states were examined by a K-Alpha XPS spectrometer (ThermoFisher, E. Grinstead, UK) with an Al K α X-ray radiation (1486.6 eV) for excitation. The crystal structures were checked by the powder X-ray diffraction (XRD) pattern (Rigaku Dmax-2000 diffractometer) using Cu K α radiation. The UV-vis absorption spectra were recorded on a Lambda950 UV/Vis/NIR spectrometer. Fourier transform infrared (FT-IR) analysis was conducted in the form of KBr pellets with a Nicolet 670 FT-IR spectrometer. Raman experiments were performed by a Renishaw Raman system model 1000 spectrometer equipped with a CCD detector, performed with a He/Ne laser at a wavelength of 633 nm. Thermogravimetric analysis (TGA) was carried out in air, using NETZSCH STA 449C thermogravimetric analyzer. The samples were heated from room temperature to 900 °C at the heat rate of 10 K min⁻¹.

2.4 Electrochemical measurements

All electrochemical experiments were performed on a CHI660b electrochemical workstation (CH Instruments, Chenhua Co., Shanghai, China). A standard

three-electrode system was used for all electrochemical experiments, which includes a Pt wire as counter electrode, a saturated calomel electrode (SCE) as reference electrode, and a bare modified glassy carbon electrode (GCE, 3 mm in diameter) or rotating disk electrode (RDE, 4 mm in diameter) as working electrode. Moreover, the RDE experiments were carried out on a PAR model 616 RDE. All the potentials here were converted to the values with reference to the reversible hydrogen electrode (RHE). The electrochemical measurements were carried out at room temperature.

For the construction of the modified electrodes, 2.3 mg of the sample was dispersed into 1.0 mL of water to form a homogeneous suspension by ultrasonication for 60 min. Then, 8 and 15 μL of the suspensions were dropped onto the GCE and RDE and dried in air, respectively, followed by casting 6 μL of Nafion (0.5 wt%) on the electrode surfaces. The Nafion acted as an adhesive to tightly combine the deposits with the electrode surfaces. The Pt-rGO and commercial Pt/C catalysts modified electrodes were prepared under the same conditions.

The electrochemically active surface area (EASA) of a catalyst can be estimated via CO-stripping voltammograms in 0.5 M H_2SO_4 .²¹ The ORR polarization curves were recorded using linear sweep voltammetry (LSV) in oxygen-saturated electrolyte (0.1 M HClO_4) with a sweep rate of 10 mV s^{-1} at different rotation speeds ranging from 100 to 2500 rpm. Furthermore, the Pt loading is 0.026 mg cm^{-2} for the PtAu-rGO, 0.048 mg cm^{-2} for the Pt-rGO, and 0.032 mg cm^{-2} for the commercial Pt/C catalysts modified RDE, respectively. The catalytic activity and stability tests were carried out by cyclic voltammetry and chronoamperometry in 1.0 M KOH,

respectively, using methanol oxidation as a model system. And the durability of the PtAu-rGO is further examined in N₂-purged 0.5 M H₂SO₄ by applying 400 cyclic potential sweeps at a scan rate of 50 mV s⁻¹.

3. Results and discussion

Morphologies of the standard sample were examined by low- (Figure 1A) and medium- (Figure 1B) magnification TEM images. The products contain plenty of well-defined popcorn-like PtAu nanoparticles with an average diameter of 35.3 nm (inset in Figure 1B), which are uniformly anchored on the surface of the rGO nanosheets. Besides, the polycrystalline nature of the PtAu particles is demonstrated by the SAED pattern (inset in Figure 1A). Moreover, each nanoparticle is indeed three dimensionally interconnected porous structures with rough surface, composing tens of much smaller grains as building units with the average diameter of around 5 nm.

Figure 1C shows the HAADF-STEM elemental mapping images of one single nanoparticle, revealing the formation of Pt-Au alloy in the nanostructures. The corresponding elemental line scanning analysis (Figure 1D) illustrates that Au is more abundant than Pt at the inner region, probably owing to the higher reduction potential of AuCl₄⁻ (0.930 V vs. RHE) than that of PtCl₆²⁻ (0.726 V vs. RHE). The formation mechanism of the PtAu alloy is assumed to be initiated by the predominant nucleation of Au, followed by co-reduction of residual AuCl₄⁻ and PtCl₆²⁻ ions on the surface of the Au-enriched seeds.²⁵ Additionally, the Pt atoms located in the center and edge are relatively abundant than those located in the other regions (Figure 1D). It might be

ascribed to the specific popcorn-like nanostructures.

In order to further investigate the detail structure information of the PtAu nanoparticles, high resolution TEM (HRTEM) images were presented (Figure 2). The d-spacing values of the lattice fringes determined from the marked regions are 0.230 and 0.200 nm, corresponding to the (111) and (200) planes of the face-centered cubic (fcc) PtAu alloy, respectively.⁹ Moreover, their (111) d-spacing value is located between individual Pt (0.227 nm, JCPDS 04-0802) and Au (0.236 nm, JCPDS 04-0784). The TEM image of the commercial 10% Pt/C catalysts (Figure S1A, Supporting Information) displays that many small Pt particles are evenly distributed on the carbon, with the average diameter of ca. 5.6 nm. The corresponding XRD pattern (Figure S1B, Supporting Information) also demonstrate the Pt/C structure, in which the diffraction peaks at 39.82°, 46.17°, 67.67°, 81.37°, 86.09°, and 26.31° are assigned to the (111), (200), (220), (311), and (222) planes of the fcc Pt and C (002) plane.²⁶ Only using H₂PtCl₆ (Figure S2A, Supporting Information) or H₂AuCl₄ (Figure S2B, Supporting Information) as precursors, smaller Pt nanoparticles or network-like Au nanowires are poorly dispersed on the rGO surfaces, rather than the popcorn-like nanostructures. Meanwhile, the absence of PVP yields heavily aggregated popcorn-like PtAu nanoparticles (Figure S3, Supporting Information), revealing the key role of PVP in the formation of the well-dispersed PtAu nanoparticles.

The oxidation states of the PtAu-rGO were analyzed by XPS analysis (Figure 3). The XPS survey spectrum is dominated by the signals of Pt, Au, C, N, and O elements

(Figure 3A). The binding energies of 73.83 and 70.64 eV correspond to the Pt 4f_{5/2} and Pt 4f_{7/2} (Figure 3B), which can be divided into two pairs of peaks at around 74.38 and 70.80, 75.53, and 72.55 eV, indicating the presence of metallic Pt and PtO/Pt(OH)₂.²⁶ From their peak intensity, we can conclude that Pt⁰ is the predominant specie. Similarly, the binding energies of 87.08 and 83.43 eV in the high-resolution XPS region (Figure 3C) are attributed to the Au 4f_{5/2} and Au 4f_{7/2}, respectively. These peaks are similar to those of metallic Au, confirming the zerovalent state of Au.²⁷ Additionally, the binding energy of 285.0 eV is corresponding to the C 1s (Figure 3D), which is fitted into four peaks at 284.58, 285.23, 286.24, and 288.08 eV, assigning to C–C (sp²), C–O, C=O, and O–C=O groups, respectively.¹⁹ Particularly, the epoxy and hydroxyl groups are obviously decreased, compared with the GO sample,²⁸ revealing effective reduction of the GO to rGO. The XPS measurements demonstrate the formation of the PtAu-rGO in the present synthesis.

The XRD pattern indicates the formation of the PtAu-rGO (Figure 4A, curve a), where the representative diffraction peaks at 39.07°, 45.06°, 65.51°, and 78.69° are matched well with the (111), (200), (220), and (311) planes of the fcc PtAu alloy.²⁹ For comparison, XRD spectra of individual Au (curve b) and Pt (curve c) nanoparticles are offered. Notably, the (111) diffraction peak of the PtAu nanoparticles coincidentally locates between single Au and Pt, which is in good agreement with the HRTEM data, further confirming the PtAu alloy feature. Besides, the lattice parameter of the PtAu nanoparticles is ca. 0.39927 nm, which lies between the bulk Pt (JCPDS-04-0802, a = 0.39030 nm) and Au (JCPDS-04-0784, a = 0.40494

nm), suggesting the incorporation of Pt and Au atoms to form PtAu alloy. The composition of the alloy would be estimated from Vegard's law, $a = a_A^0(1 - X) + a_B^0(X)$, where X is the mole fraction of component B, and a_A^0 and a_B^0 are the lattice parameters of individual A and B, respectively.³⁰ The calculated molar ratio of Pt/Au is 38.7:61.3 in the binary alloy.

The line broadening of the (220) diffraction peak is used to calculate the average crystallite size based on Scherrer's equation, $L = (0.9 \lambda) / (\beta_{1/2} \cos\theta)$, where λ is the wavelength of the X-ray (1.5406 Å), θ is the angle at the position of the peak maximum, and $\beta_{1/2}$ is the width of the diffraction peak at half height in radians.^{31, 32} The metal crystallite size was calculated to be 4.5, 3.8, and 3.9 nm for the PtAu-rGO, Pt-rGO, and Au-rGO, respectively. The crystallite size calculated from the XRD test is consistent with the PtAu nanoparticles (~5 nm) obtained from the HRTEM experiments. This phenomenon is similar to those reported in the literature.³³ In addition, the peak at 21.6° is originated from the (002) planes of hexagonal structure of graphene, unlike the GO (curve d) with a peak located at 10.0° corresponding to the oxygenated functional groups.³⁴ These observations indicate the effective reduction of GO to rGO by NaBH₄.¹⁹

Figure 4B shows the UV-vis spectra of the PtAu-rGO (curve a), Pt-rGO (curve b), Au-rGO (curve c), GO (curve d), and rGO (curve e). There is a strong peak at 230 nm for the GO sample, corresponding to the $\pi \rightarrow \pi^*$ transition of aromatic C–C bonds. Meanwhile, a smaller shoulder peak is emerged at 301 nm, which can be ascribed to the $n \rightarrow \pi^*$ transition of the C=O bonds.³⁶ However, the absorption peak at 230 nm red

shifts to 260 nm for the PtAu-rGO, Pt-rGO, and Au-rGO, which is similar to that of the rGO, indicating the formation of rGO in the present synthesis. For the Au-rGO, the pronounced absorption peak at 530 nm corresponds to the surface plasmon resonance of Au,³⁷ which is much higher than that of the PtAu-rGO, but different from that of the Pt-rGO. These results demonstrate the emergence of Pt-Au alloy in the PtAu-rGO nanocomposites.

Figure 4C displays the FT-IR spectra of the PtAu-rGO (curve a), Pt-rGO (curve b), and GO (curve c). For the GO sample, the characteristic stretching peaks of C–OH (1040 cm^{-1}), C–O (1230 cm^{-1}), O–H (1400 cm^{-1}), and C=O (1730 cm^{-1}) groups are clearly observed, demonstrating that graphite was effectively oxidized to GO under the standard conditions.³⁸ After reduction by NaBH_4 , most of the peaks from the oxygen-containing groups decreased obviously, indicating the GO was significantly deoxygenated and the rGO was formed accordingly.³⁹

Raman spectroscopy is usually applied to monitor the structural changes in graphene-based materials. Raman spectra of the PtAu-rGO (curve a), Pt-rGO (curve b), and GO (curve c) are displayed (Figure 4D). In each case, the two distinguished characteristic peaks at 1340 and 1596 cm^{-1} correspond to the *D* band correlated with the A_{1g} breathing mode of the disordered graphite structures and *G* band related with the doubly degenerate E_{2g} of graphite.⁴⁰ Using the *D/G* peak area ratio (I_D/I_G , 0.82) in the GO sample as a reference, the I_D/I_G ratios are increased to 1.83 for the PtAu-rGO and 1.82 for the Pt-rGO, respectively. These results manifest the formation of smaller in-plane sp^2 domains after the reduction of GO and again confirm the formation of the

rGO.⁴⁰

The weight loss of the sample is simultaneously examined by TGA/DSC (Figure 5). The PtAu-rGO (curve a) exhibits a small weight loss below 100 °C, corresponding to the escaped water molecules absorbed between the rGO nanosheets. And the steady weight loss from 200 to 400 °C is assigned to the destruction of oxygenated functional groups remained in the rGO.⁴¹ After a significant drop in mass at around 410 °C, the carbon skeleton of the rGO is completely combusted to CO or CO₂.²⁸ In contrast, the GO shows a dramatic mass loss accompanied by an exothermic DSC peak at 200 °C, which is much higher than those of the PtAu-rGO (curve a) and Pt-rGO (curve b), revealing the decrease of the oxygen-containing functional groups in the rGO. Additionally, the metal loading is 78% for the PtAu-rGO (evaluated from the residual mass), which is larger than the Pt-rGO with a value of 32.6%.

Glucosamine is used here as a reducing agent and a structure-directing agent. The formation mechanism can be inferred as follows: both PtCl₆²⁻ and AuCl₄⁻ ions firstly bind to the amino group of glucosamine, resulting in the formation of amino-AuCl₄⁻/PtCl₆²⁻ complexes.⁴² Simultaneously, the adsorbed PtCl₆²⁻ and AuCl₄⁻ ions are reduced to Pt and Au atoms immediately by the aldehyde group of glucosamine. Meanwhile, to stabilize the newly generated PtAu nanocrystals, the released glucosamine would selectively adsorbed on the (110)/(100) crystal planes as the surface energies increase in the order of (111) < (100) << (110).⁴³ Such behaviors would block the crystal growth along the (110)/(100) directions and promote the anisotropic growth on the (111) directions, causing the predominant orientation of the

(111) planes, as displayed in the XRD pattern.

Furthermore, the higher reduction potential of AuCl_4^- (0.930 V vs. RHE) than that of PtCl_6^{2-} (0.726 V vs. RHE) leads to the relatively abundant Au atoms in the inner of the PtAu nanoparticles. In addition, the existence of PVP is essential to the formation of uniform PtAu nanoparticles, which is served as a stabilizing agent to efficiently prevent the PtAu nanoparticles from aggregation.^{44, 45}

For Pt-based catalysts, CO is a major poisoning intermediate in alcohol oxidation process, and thereby CO stripping serves as a model probe to evaluate their CO tolerance. Figure 6 provides the CO stripping voltammograms of the PtAu-rGO (Figure 6A), Pt-rGO (Figure 6B), and commercial Pt/C catalysts modified electrodes (Figure 6C). It is clear that the hydrogen desorption peaks are completely suppressed from 0.1 to 0.2 V (vs. RHE) in the first positive-going scan, owing to the saturated coverage of CO on the active sites.⁴⁶ With the oxidation removal of the adsorbed CO-like intermediates, the hydrogen desorption peaks recovered in the second scan. A broad current peak located between 0.8 and 1.2 V is ascribed to the CO oxidation. Obviously, the onset potential (0.703 V) for the PtAu-rGO is relatively negative, compared with those of the Pt-rGO (0.768 V) and commercial Pt/C (0.721 V) catalysts, suggesting a better CO oxidation activity of the PtAu-rGO.

Besides, the electrochemically active surface area (EASA) is calculated from the CO stripping voltammograms,⁴⁷ which is about $75.27 \text{ m}^2 \text{ g}^{-1}$ for the PtAu-rGO. This value is higher than those of the Pt-rGO ($17.94 \text{ m}^2 \text{ g}^{-1}$) and commercial Pt/C ($7.23 \text{ m}^2 \text{ g}^{-1}$) catalysts. The negative shift of the onset potential and the larger EASA are

attributed to the special structures of the PtAu-rGO nanocomposites.

The ORR measurements were performed in O₂-saturated 0.1 M HClO₄ at a rotation rate of 1600 rpm. Figure 7A shows the polarization curves of the PtAu-rGO (curve a), Pt-rGO (curve b), and commercial Pt/C (curve c) catalysts modified electrodes. In each case, the diffusion-limiting currents are obtained below 0.30 V, whereas a mixed kinetic-diffusion controlled region appears from 0.40 to 0.85 V. Clearly, the PtAu-rGO exhibits a more positive onset potential (0.83 V), compared with those of the Pt-rGO (0.75 V) and commercial Pt/C (0.77 V) catalysts. The half-wave potentials of the PtAu-rGO, Pt-rGO, and commercial Pt/C catalysts are 0.74, 0.57, and 0.54 V, respectively. These results mean that the higher electrocatalytic activity of the PtAu-rGO, compared with the Pt-rGO and commercial Pt/C catalysts.

The kinetic current density (i_k) represents the intrinsic activity of catalysts, which is a better indicator of the performance of a catalyst.⁴⁸ The kinetic current density is analyzed on the basis of the Koutecky-Levich equation.⁴⁹ To further compare the ORR activity, the kinetic currents are normalized with respect to both the EASA and the loading amount of Pt.

As shown in Figure 7B, the PtAu-rGO shows a specific activity of 0.40 mA cm_{Pt}⁻² at 0.6 V (vs. RHE), which is 2.5 and 1.1 times larger than those of the Pt-rGO (0.16 mA cm_{Pt}⁻²) and commercial Pt/C (0.35 mA cm_{Pt}⁻²) catalysts, respectively. Besides, the mass activity of the PtAu-rGO is 0.30 mA μg_{Pt}⁻¹, which is nearly 10.7 and 20.0 times higher than those of the Pt-rGO (0.028 mA μg_{Pt}⁻¹) and commercial

Pt/C (0.015 mA $\mu\text{g}_{\text{Pt}}^{-1}$) catalysts, respectively. Moreover, the activity of the PtAu-rGO (0.40 mA $\text{cm}_{\text{Pt}}^{-2}$) is also higher, compared with those of the Pt-Pd alloy nanoflowers (0.38 mA $\text{cm}_{\text{Pt}}^{-2}$),⁵⁰ Au-PtCu core-shell nanoparticles (0.26 mA $\text{cm}_{\text{Pt}}^{-2}$),⁵¹ and Pt₃Ni nanopolyhedra (0.11 mA $\mu\text{g}_{\text{Pt}}^{-1}$).⁵²

More detailed investigations on the ORR features have been performed by altering the rotation speed of the modified RDE. Figure 8A profiles a group of the polarization curves at different rotation rates, which are normalized by the geometrical area of the electrodes. Figure 8B provides the corresponding Koutecky-Levich plot obtained from the inverse current density (j^{-1}) as a function of the inverse of the square root of the rotation rate ($\omega^{-1/2}$) at 0.6 V. The good linearity and parallelism of the plot usually indicate the first-order kinetics with respect to molecular oxygen.⁵³ The electron transfer number can be calculated from the Koutecky-Levich equation:

$$i_d = B \times \omega^{1/2} \quad (1)$$

$$B = 0.62 \times n \times F \times A \times D^{2/3} \times \nu^{-1/6} \times C_{O_2} \quad (2)$$

here, n is the number of transferred electrons in the reaction, F is the Faraday constant (96485 C mol^{-1}), A is the geometrical area (0.1256 cm^2), D is the oxygen diffusivity ($1.93 \times 10^{-5} \text{cm}^2 \text{s}^{-1}$), ν is the kinematic viscosity of the electrolyte ($1.009 \times 10^{-2} \text{cm}^2 \text{s}^{-1}$), and C_{O_2} is the oxygen solubility ($1.26 \times 10^{-3} \text{molL}^{-1}$).^{51, 54} By applying these parameters to the equation (2), $B = 0.015 n$. From the slope of the Koutecky-Levich plot, the n is calculated to be 3.92 for the PtAu-rGO, implying the reduction of O₂ to H₂O via the four-electron pathway.⁵⁵

In order to investigate the electrocatalytic performance of the PtAu-rGO for methanol oxidation, the cyclic voltammograms of the PtAu-rGO (curve a, Pt loading: 0.046 mg cm^{-2}), Pt-rGO (curve b, Pt loading: 0.085 mg cm^{-2}), and commercial Pt/C (curve c, Pt loading: 0.042 mg cm^{-2}) catalysts were recorded in 1.0 M KOH containing 1 M methanol (Figure 9A). In all cases, there are two anodic peaks observed in the forward and reverse scans, which correspond to methanol oxidation and incompletely oxidized carbonaceous species.

Specifically, the onset anodic potential for methanol oxidation is -0.21 V for the PtAu-rGO (curve a), which is more negative than the Pt-rGO (curve b, -0.17 V) and commercial Pt/C (curve c, -0.19 V) catalysts. The negative shift of the onset potential indicates significant enhancement in the kinetics of methanol oxidation reaction.

Methanol oxidation is characterized by well-separated anodic peaks in the forward and reverse scans. The magnitude of the forward anodic peak current density (j_f) is proportional to the reaction activity. The current density of the PtAu-rGO (curve a) is 28.95 mA cm^{-2} , which is almost 4.6 and 34.1 folds higher than the Pt-rGO (curve b, 6.36 mA cm^{-2}) and commercial Pt/C (curve c, 0.85 mA cm^{-2}) catalysts, respectively. Meanwhile, nearly no CO poisoning peak is detected in the case of the PtAu-rGO. And the ratio of the j_f to the reverse oxidation peak current density (j_r) of the PtAu-rGO (j_f/j_r) is 29.25, which is much higher than the Pt-rGO (18.68) and commercial Pt/C (10.15) catalysts, indicating that the PtAu-rGO suffers little from poisoning and deactivation. These data further confirm the improved electrocatalytic performances of the PtAu-rGO, as demonstrated in Table S1 (Supporting Information)

and Figure 9B. More impressively, it is found that the activity of the PtAu-rGO is higher than those of the Pt-based nanostructures such as Pt nanoflowers/rGO ($133.43 \text{ mA mg}_{\text{Pt}}^{-1}$),⁵⁶ mesoporous PtRu alloy (85 mA mg^{-1}),⁵⁷ Pt-Pd nanoflowers ($0.3 \text{ mA cm}_{\text{Pt}}^{-2}$),⁵⁰ and Ag@Pt core-shell nanoparticles ($150 \text{ mA mg}_{\text{Pt}}^{-1}$).⁵⁸ It is ascribed to a large number of active sites available for the PtAu-rGO, as supported by the larger EASA from the CO stripping measurements.

The stability of the PtAu-rGO (curve a), Pt-rGO (curve b), and commercial Pt/C (curve c) catalysts modified electrodes was examined by chronoamperometry in 1.0 M KOH containing 1.0 M methanol. The anodic current density of each catalyst initially exhibits a rapid decay because of the formation of intermediate species during methanol oxidation (Figure 10). Moreover, the PtAu-rGO shows a higher initial current and much slower current decay, compared with those of the Pt-rGO and commercial Pt/C catalysts. At the end of the 6000 s, the oxidation current on the PtAu-rGO is still the highest, further revealing relatively better tolerance to the CO-like intermediates and higher catalytic property of the PtAu-rGO.

The durability of the PtAu-rGO was further verified by cyclic voltammetry in N_2 -purged 0.5 M H_2SO_4 , where the EASA (determined from the hydrogen adsorption region) is almost kept constant with a small loss of 1.2% within 400 cycles (Figure 11). The improved electrocatalytic ability, strong tolerance, and better stability of the PtAu-rGO are attributed to three factors. (i) The popcorn-like structures contribute larger EASA. And the abundant atomic steps, edges, and corner atoms in the PtAu branches would act as highly active sites for methanol oxidation.⁵⁹⁻⁶¹ (ii) Better

dispersion of the PtAu nanoparticles on the rGO nanosheets that enlarges surface area and facilitates electron transport. (iii) The higher electronegativity of Au (2.54) relative to Pt (2.28). The electron transfer from Au to adjacent Pt causes an increase of the 5d vacancies in Pt and facilitates methanol adsorption on the active sites of Pt, which are favorable for methanol oxidation.

4. Conclusion

A facile and mild method was developed for fabrication of the PtAu-rGO with high quality in alkaline media, using glucosamine as a reducing agent. The as-formed PtAu nanoparticles showed well-defined popcorn-like alloy structures and well dispersion, which exhibited the improved electrocatalytic property and a predominant four-electron pathway based on the Koutecky-Levich plot in ORR, compared with the Pt-rGO and commercial Pt/C catalysts. Besides, the PtAu-rGO displayed the improved catalytic activity and stability for methanol oxidation. The as-developed method provides a promising pathway for the design of highly efficient electrocatalysts in ORR and methanol oxidation.

Acknowledgement

This work was financially supported by the NSFC (Nos. 21175118, 21275130 and 21275131), and Zhejiang province university young academic leaders of academic climbing project (No. pd2013055).

References

- 1 B. Lim, M. Jiang, P. H. C. Camargo, E. C. Cho, J. Tao, X. Lu, Y. Zhu and Y. Xia, *Science*, 2009, **324**, 1302-1305.
- 2 L. Wang, Y. Nemoto and Y. Yamauchi, *J. Am. Chem. Soc.*, 2011, **133**, 9674-9677.
- 3 S. Guo, S. Dong and E. Wang, *ACS Nano*, 2009, **4**, 547-555.
- 4 Y. W. Lee, M. Kim, Y. Kim, S. W. Kang, J.-H. Lee and S. W. Han, *J. Phys. Chem. C*, 2010, **114**, 7689-7693.
- 5 X. Huang, E. Zhu, Y. Chen, Y. Li, C.-Y. Chiu, Y. Xu, Z. Lin, X. Duan and Y. Huang, *Adv. Mater.*, 2013, **25**, 2974-2979.
- 6 Z. Peng and H. Yang, *J. Am. Chem. Soc.*, 2009, **131**, 7542-7543.
- 7 L. Shi, A. Wang, T. Zhang, B. Zhang, D. Su, H. Li and Y. Song, *J. Phys. Chem. C*, 2013, **117**, 12526-12536.
- 8 J. Watt, S. Cheong, M. F. Toney, B. Ingham, J. Cookson, P. T. Bishop and R. D. Tilley, *ACS Nano*, 2009, **4**, 396-402.
- 9 X. Cao, N. Wang, S. Jia, L. Guo and K. Li, *Biosens. Bioelectron.*, 2013, **39**, 226-230.
- 10 H. Atae-Esfahani, L. Wang, Y. Nemoto and Y. Yamauchi, *Chem. Mater.*, 2010, **22**, 6310-6318.
- 11 S. Guo, J. Li, S. Dong and E. Wang, *J. Phys. Chem. C*, 2010, **114**, 15337-15342.
- 12 Y. Kim, H. J. Kim, Y. S. Kim, S. M. Choi, M. H. Seo and W. B. Kim, *J. Phys. Chem. C*, 2012, **116**, 18093-18100.
- 13 Y. Kim, J. W. Hong, Y. W. Lee, M. Kim, D. Kim, W. S. Yun and S. W. Han,

- Angew Chem Int Edit*, 2010, **49**, 10197-10201.
- 14 D. Zhao and B.-Q. Xu, *Angew Chem Int Edit*, 2006, **45**, 4955-4959.
- 15 J. Luo, P. N. Njoki, Y. Lin, D. Mott, Wang and C.-J. Zhong, *Langmuir*, 2006, **22**, 2892-2898.
- 16 S. Zhou, K. McIlwrath, G. Jackson and B. Eichhorn, *J. Am. Chem. Soc.*, 2006, **128**, 1780-1781.
- 17 J. Wang, G. Yin, H. Liu, R. Li, R. L. Flemming and X. Sun, *J. Power Sources*, 2009, **194**, 668-673.
- 18 X. Wang, D. Liu, S. Song and H. Zhang, *J. Am. Chem. Soc.*, 2013, **135**, 15864-15872.
- 19 Y. Li, W. Gao, L. Ci, C. Wang and P. M. Ajayan, *Carbon*, 2010, **48**, 1124-1130.
- 20 Y. Li, X. Fan, J. Qi, J. Ji, S. Wang, G. Zhang and F. Zhang, *Nano Research*, 2010, **3**, 429-437.
- 21 J.-J. Feng, D.-L. Zhou, H.-X. Xi, J.-R. Chen and A.-J. Wang, *Nanoscale*, 2013, **5**, 6754-6757.
- 22 M. Liu, Y. Lu and W. Chen, *Adv. Funct. Mater.*, 2013, **23**, 1289-1296.
- 23 C. Huang, C. Li and G. Shi, *Energy Environ. Sci.*, 2012, **5**, 8848-8868.
- 24 W. S. Hummers and R. E. Offeman, *J. Am. Chem. Soc.*, 1958, **80**, 1339-1339.
- 25 J. W. Hong, Y. W. Lee, M. Kim, S. W. Kang and S. W. Han, *Chem. Commun.*, 2011, **47**, 2553-2555.
- 26 Z.-Z. Jiang, Z.-B. Wang, Y.-Y. Chu, D.-M. Gu and G.-P. Yin, *Energy Environ. Sci.*, 2011, **4**, 728-735.

- 27 R. Chetty, S. Kundu, W. Xia, M. Bron, W. Schuhmann, V. Chirila, W. Brandl, T. Reinecke and M. Muhler, *Electrochim. Acta*, 2009, **54**, 4208-4215.
- 28 A.-J. Wang, S.-F. Qin, D.-L. Zhou, L.-Y. Cai, J.-R. Chen and J.-J. Feng, *RSC Advances*, 2013, **3**, 14766-14773.
- 29 C. Xu, X. Wang and J. Zhu, *J. Phys. Chem. C*, 2008, **112**, 19841-19845.
- 30 J. Xu, T. Zhao, Z. Liang and L. Zhu, *Chem. Mater.*, 2008, **20**, 1688-1690.
- 31 K. T. Jacob, S. Raj and L. Rannesh, *Int. J. Mater. Res.*, 2007, **98**, 776-779.
- 32 Y. Zhao, L. Zhan, J. Tian, S. Nie and Z. Ning, *Electrochim. Acta*, 2011, **56**, 1967-1972.
- 33 C. Venkateswara Rao and B. Viswanathan, *J. Phys. Chem. C*, 2009, **113**, 18907-18913.
- 34 G. Fu, W. Han, L. Yao, J. Lin, S. Wei, Y. Chen, Y. Tang, Y. Zhou, T. Lu and X. Xia, *J. Mater. Chem.*, 2012, **22**, 17604-17611.
- 35 H.-K. Jeong, Y. P. Lee, R. J. W. E. Lahaye, M.-H. Park, K. H. An, I. J. Kim, C.-W. Yang, C. Y. Park, R. S. Ruoff and Y. H. Lee, *J. Am. Chem. Soc.*, 2008, **130**, 1362-1366.
- 36 S.-S. Li, J.-J. Lv, Y.-Y. Hu, J.-N. Zheng, J.-R. Chen, A.-J. Wang and J.-J. Feng, *J. Power Sources*, 2014, **247**, 213-218.
- 37 J.-J. Feng, H. Guo, Y.-F. Li, Y.-H. Wang, W.-Y. Chen and A.-J. Wang, *ACS Appl. Mater. Interfaces*, 2013, **5**, 1226-1231.
- 38 R. Bissessur, P. K. Y. Liu, W. White and S. F. Scully, *Langmuir*, 2006, **22**, 1729-1734.

- 39 H. Zhang, X. Xu, P. Gu, C. Li, P. Wu and C. Cai, *Electrochim. Acta*, 2011, **56**, 7064-7070.
- 40 H.-L. Guo, X.-F. Wang, Q.-Y. Qian, F.-B. Wang and X.-H. Xia, *ACS Nano*, 2009, **3**, 2653-2659.
- 41 S. Sharma, A. Ganguly, P. Papakonstantinou, X. Miao, M. Li, J. L. Hutchison, M. Delichatsios and S. Ukleja, *J. Phys. Chem. C*, 2010, **114**, 19459-19466.
- 42 A.-J. Wang, Y.-F. Li, M. Wen, G. Yang, J.-J. Feng, J. Yang and H.-Y. Wang, *New J. Chem.*, 2012, **36**, 2286-2291.
- 43 M. Chen, B. Wu, J. Yang and N. Zheng, *Adv. Mater.*, 2012, **24**, 862-879.
- 44 J.-J. Lv, J.-N. Zheng, S.-S. Li, L.-L. Chen, A.-J. Wang and J.-J. Feng, *J. Mater. Chem. A*, 2014, DOI: 10.1039/c3ta14304j.
- 45 J. Xiao and L. Qi, *Nanoscale*, 2011, **3**, 1383-1396.
- 46 W. Sugimoto, K. Aoyama, T. Kawaguchi, Y. Murakami and Y. Takasu, *J. Electroanal. Chem.*, 2005, **576**, 215-221.
- 47 A. Pozio, M. De Francesco, A. Cemmi, F. Cardellini and L. Giorgi, *J. Power Sources*, 2002, **105**, 13-19.
- 48 Z. Peng, J. Wu and H. Yang, *Chem. Mater.*, 2009, **22**, 1098-1106.
- 49 W. Chen and S. Chen, *Angew Chem Int Edit*, 2009, **48**, 4386-4389.
- 50 G. Fu, K. Wu, J. Lin, Y. Tang, Y. Chen, Y. Zhou and T. Lu, *J. Phys. Chem. C*, 2013, **117**, 9826-9834.
- 51 C. Hsu, C. Huang, Y. Hao and F. Liu, *Phys. Chem. Chem. Phys.*, 2012, **14**, 14696-14701.

- 52 J. Zhang, H. Yang, J. Fang and S. Zou, *Nano Lett.*, 2010, **10**, 638-644.
- 53 J. Zhang, Y. Mo, M. B. Vukmirovic, R. Klie, K. Sasaki and R. R. Adzic, *J. Phys. Chem. B*, 2004, **108**, 10955-10964.
- 54 C. Xu, Y. Zhang, L. Wang, L. Xu, X. Bian, H. Ma and Y. Ding, *Chem. Mater.*, 2009, **21**, 3110-3116.
- 55 J. Xu, G. Fu, Y. Tang, Y. Zhou, Y. Chen and T. Lu, *J. Mater. Chem.*, 2012, **22**, 13585-13590.
- 56 Z. Yao, M. Zhu, F. Jiang, Y. Du, C. Wang and P. Yang, *J. Mater. Chem.*, 2012, **22**, 13707-13713.
- 57 E. A. Franceschini, G. A. Planes, F. J. Williams, G. J. A. A. Soler-Illia and H. R. Corti, *J. Power Sources*, 2011, **196**, 1723-1729.
- 58 C. Li and Y. Yamauchi, *Phys. Chem. Chem. Phys.*, 2013, **15**, 3490-3496.
- 59 Z.-Y. Zhou, Z.-Z. Huang, D.-J. Chen, Q. Wang, N. Tian and S.-G. Sun, *Angew Chem Int Edit*, 2010, **49**, 411-414.
- 60 S. W. Lee, S. Chen, W. Sheng, N. Yabuuchi, Y.-T. Kim, T. Mitani, E. Vescovo and Y. Shao-Horn, *J. Am. Chem. Soc.*, 2009, **131**, 15669-15677.
- 61 Mahmoud, C. E. Tabor, M. A. El-Sayed, Y. Ding and Z. L. Wang, *J. Am. Chem. Soc.*, 2008, **130**, 4590-4591.

Captions

Figure 1. TEM images of the PtAu-rGO(A, B), HAADF-STEM-EDS mapping images of a PtAu nanodendrite (C), and the HAADF-STEM image and cross-sectional compositional line profiles (D). Insets show the corresponding SEAD pattern in image (A) and the size distribution in image (B).

Figure 2. HRTEM images of the PtAu-rGO (A, B).

Figure 3. Survey (A), and high-resolution Pt $4f_{5/2}$ and Pt $4f_{7/2}$ (B), Au $4f_{5/2}$ and Au $4f_{7/2}$ (C), and C 1s (D) XPS spectra of the PtAu-rGO.

Figure 4. XRD patterns (A) of the PtAu-rGO (curve a), Au (curve b), Pt (curve c), and GO (curve d). UV-vis absorption spectra (B) of the PtAu-rGO (curve a), Pt-rGO (curve b), Au-rGO (curve c), GO (curve d), and rGO (curve e). FT-IR (C) and (D) Raman spectra of the PtAu-rGO (curve a), Pt-rGO (curve b), and GO (curve c).

Figure 5. (A) TGA curves of the PtAu-rGO (curve a), Pt-rGO (curve b), and GO (curve c). The corresponding DSC curves of the PtAu-rGO (curve a'), Pt-rGO (curve b'), and GO (curve c').

Figure 6. CO-stripping voltammograms of the PtAu-rGO (A), Pt-rGO (B), and commercial Pt/C (C) catalysts in 0.5 M H₂SO₄ at a scan rate of 50 mV s⁻¹.

Figure 7. (A) ORR polarization curves of the PtAu-rGO (curve a), Pt-rGO (curve b), and commercial Pt/C (curve c) catalysts modified electrodes in O₂-saturated 0.1 M HClO₄ with the rotation rate of 1600 rpm and a scan rate of 10 mV s⁻¹. (B) The corresponding specific and mass kinetic current densities at 0.6 V.

Figure 8. (A) The polarization curves of ORR of the PtAu-rGO modified electrodes in O₂-saturated 0.1 M HClO₄ at different rotation rates. Scan rate: 10 mV s⁻¹. (B) The corresponding Koutecky-Levich plot at 0.6 V.

Figure 9. (A) The cyclic voltammograms of the PtAu-rGO (curve a), Pt-RGO (curve b), and commercial Pt/C (curve c) catalysts modified electrodes in 1.0 M KOH containing 1.0 M methanol. (B) The corresponding current densities and mass activities.

Figure 10. The chronoamperometric curves of the PtAu-rGO (curve a), Pt-RGO (curve a), and commercial Pt/C (curve c) catalysts modified electrodes in 1.0 M KOH containing 1.0 M methanol by applying a potential of -0.1 V (vs. RHE). Inset shows the high-magnification chronoamperometric curves of the Pt-rGO (curve b) and commercial Pt/C catalysts (curve c).

Figure 11. The cyclic voltammograms curves of the PtAu-rGO modified electrode before and after 400 cycles in N₂-saturated 0.5 M H₂SO₄.

Figures

Figure 1

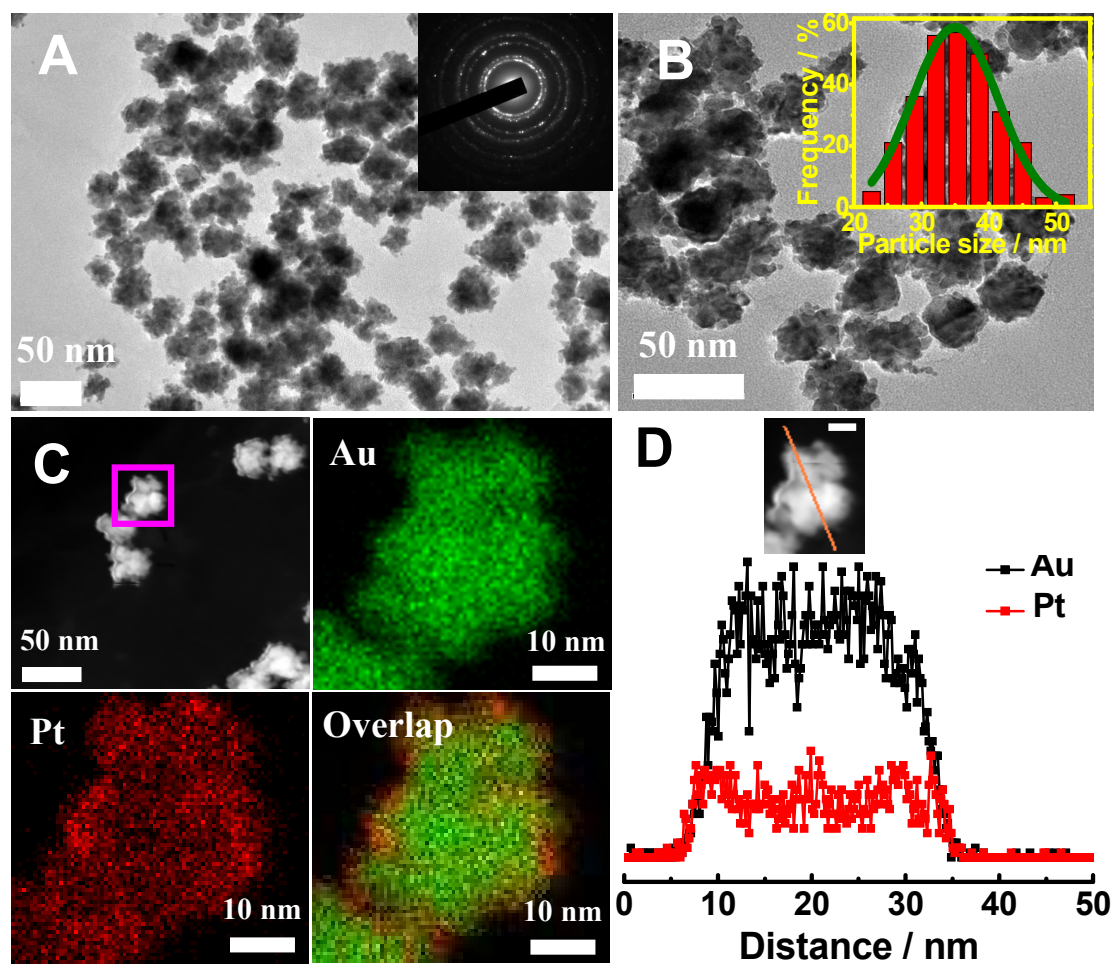


Figure 2

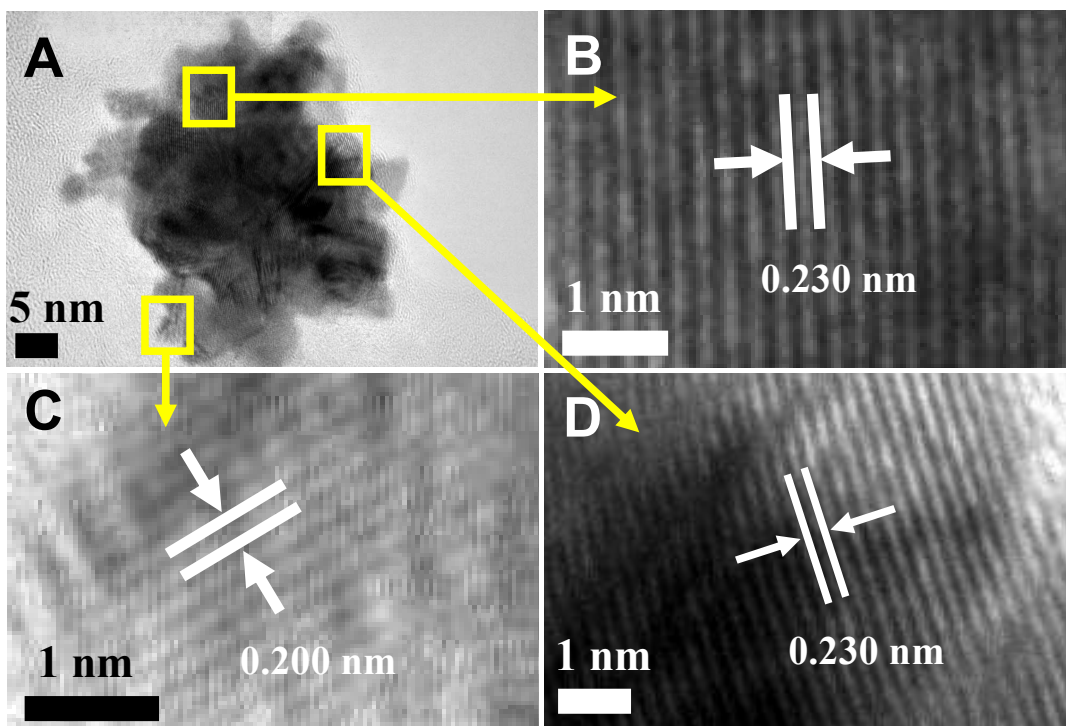


Figure 3

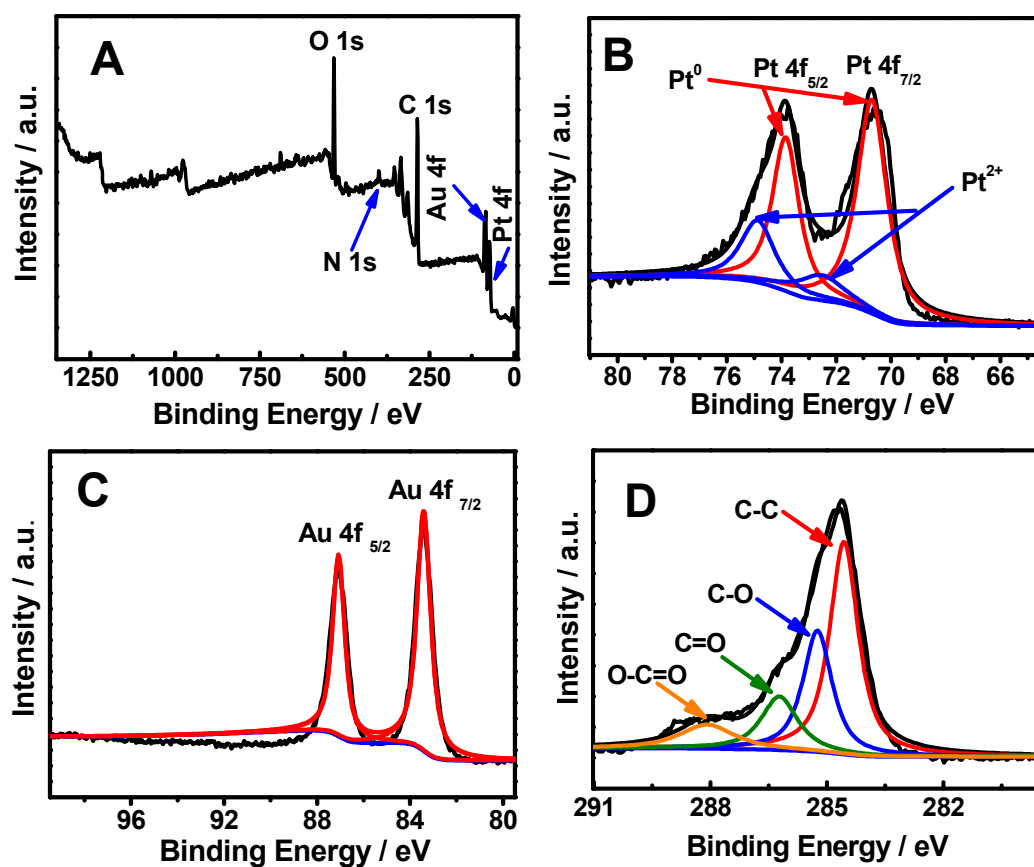


Figure 4

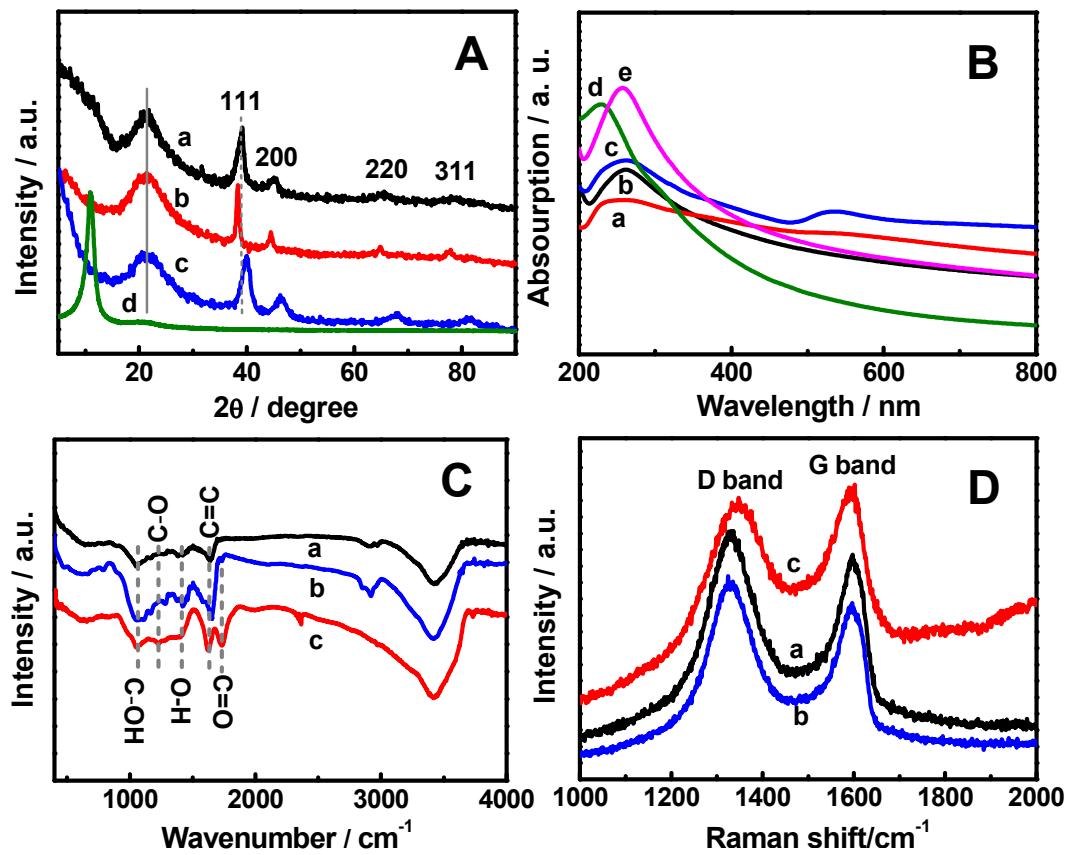


Figure 5

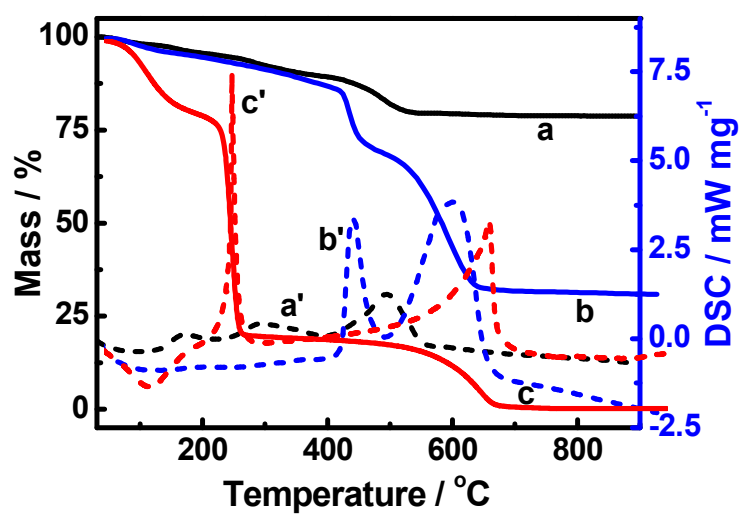


Figure 6

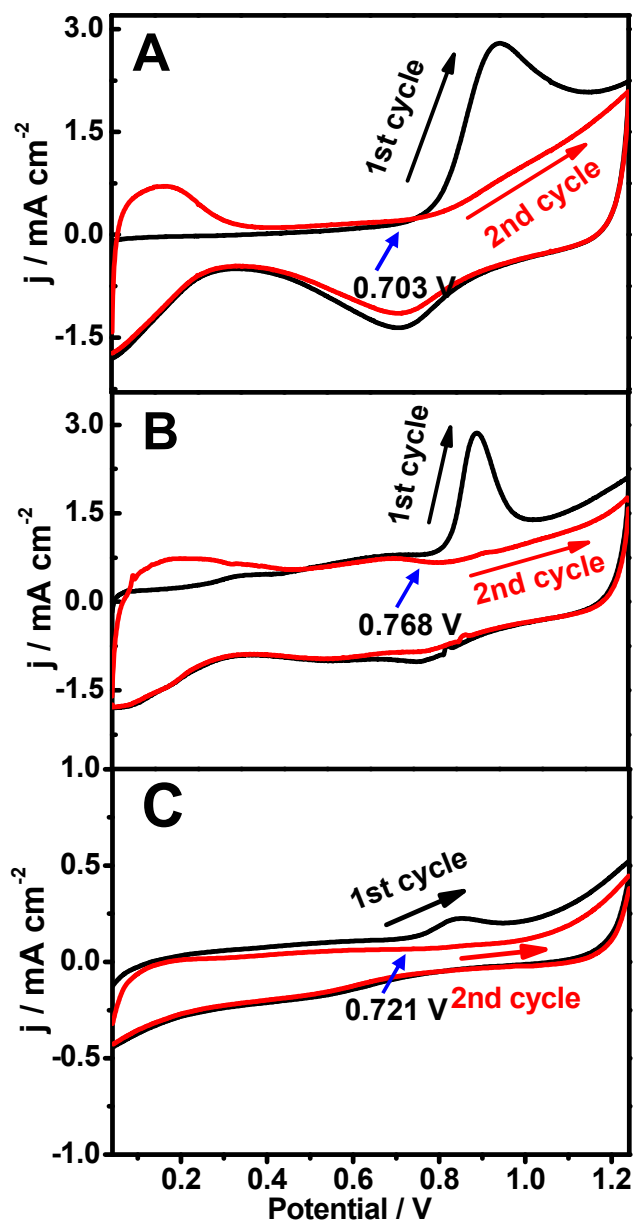


Figure 7

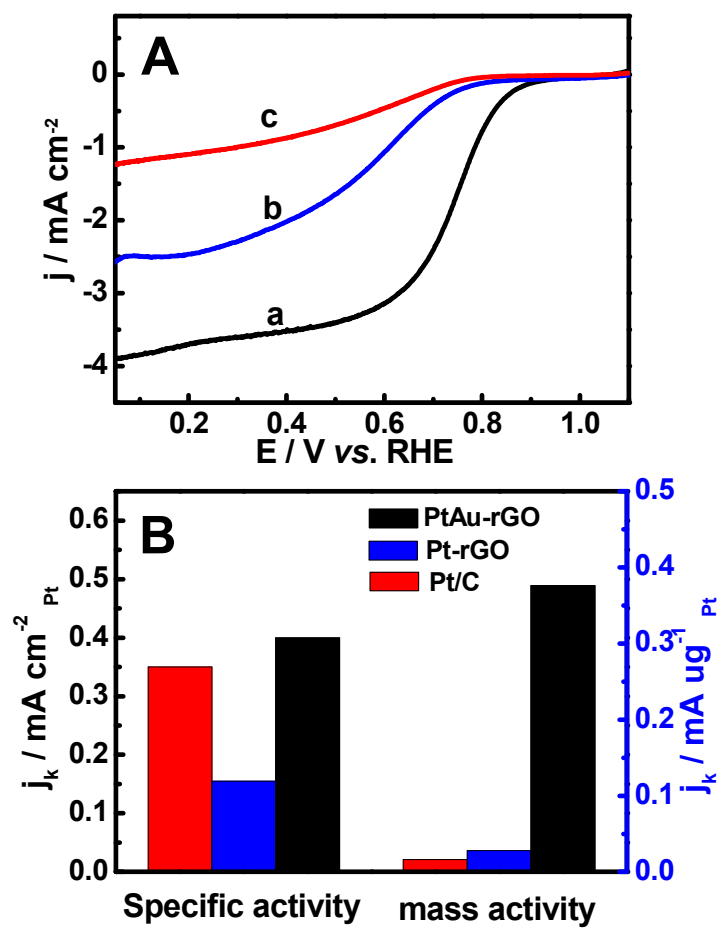


Figure 8

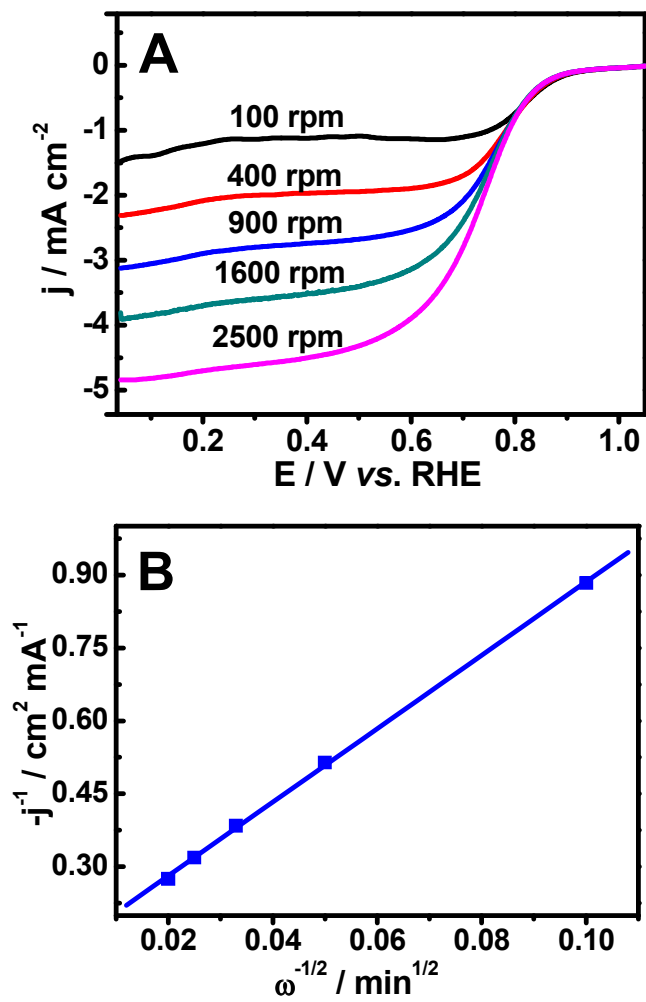


Figure 9

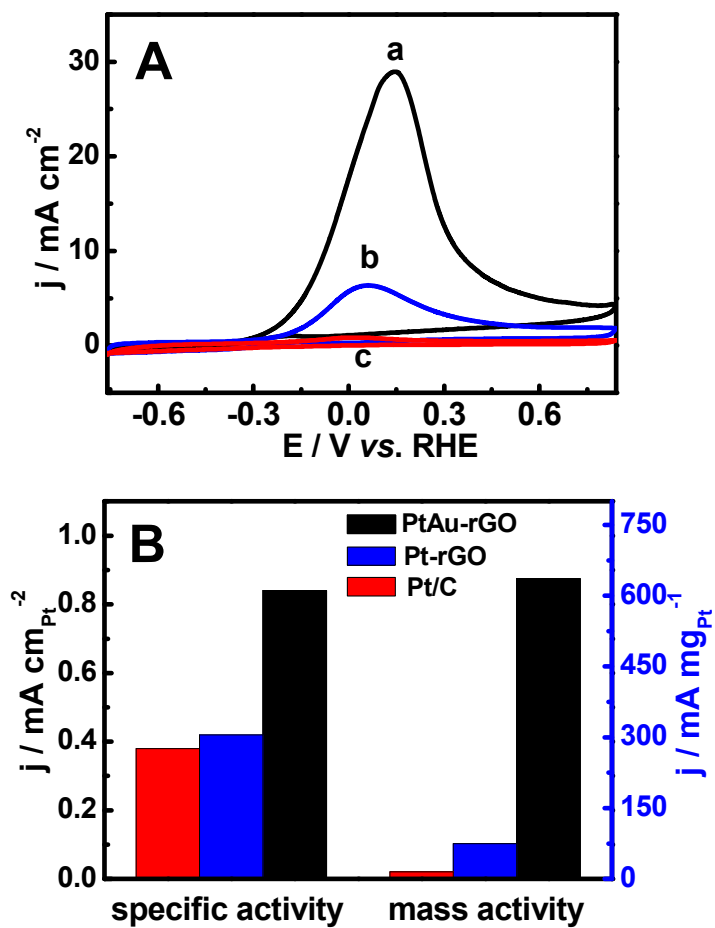


Figure 10

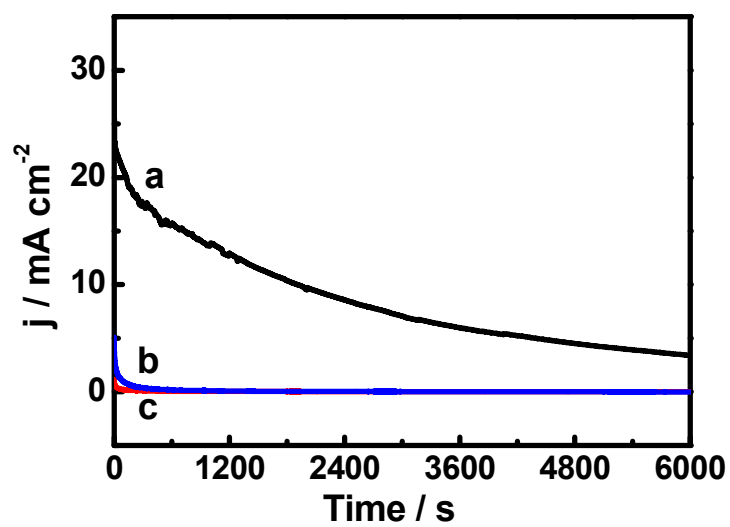
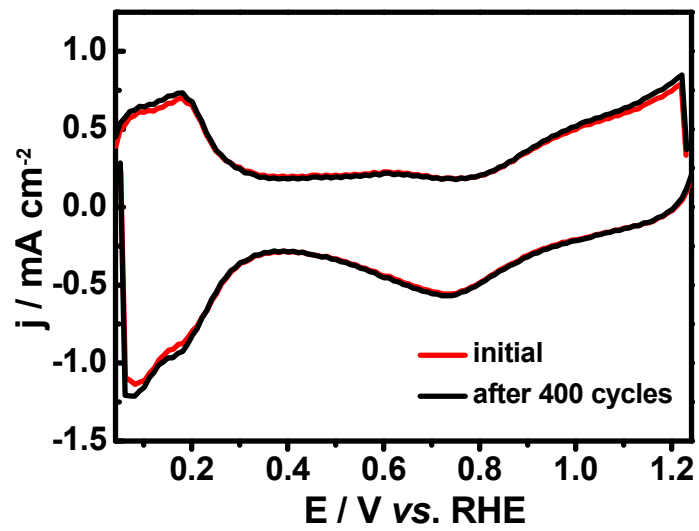
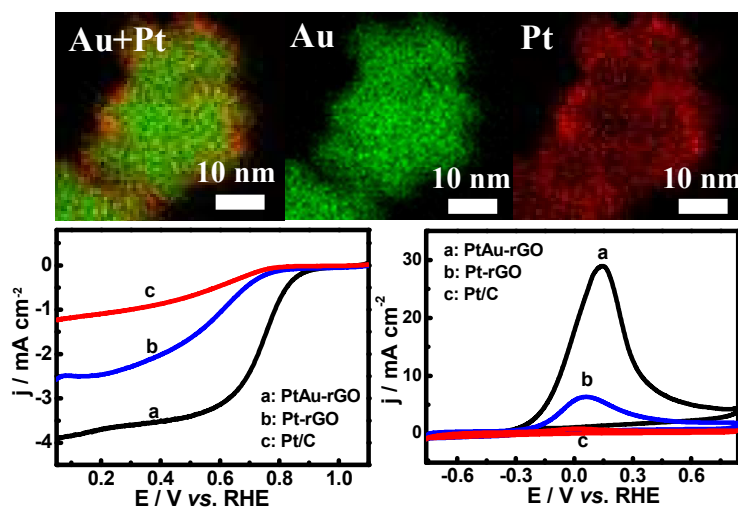


Figure 11



Graphic Abstract



Popcorn-like PtAu nanoparticles were fabricated using glucosamine as a reducing agent and further supported on rGO by ultrasonication. The as-prepared nanocomposites showed the enhanced electrocatalytic performance for ORR and methanol oxidation.